Biosensors and Bioelectronics 254 (2024) 116241

Contents lists available at ScienceDirect

Biosensors and Bioelectronics

journal homepage: www.elsevier.com/locate/bios

Electrochemiluminescence biosensor for specific detection of pancreatic ductal carcinoma through dual targeting of MUC1 and miRNA-196a

Yuxuan Chen [a], Zhuoxin Ye [a], Mo Ma [a,b], Jukun Yang [a], Ruiyan Liu [a], Yan Zhang [a], Pinyi Ma [a,**], Daqian Song [a,*]

[a] College of Chemistry, Jilin Province Research Center for Engineering and Technology of Spectral Analytical Instruments, Jilin University, Qianjin Street 2699, Changchun, 130012, China
[b] School of Pharmacy, Jilin University, Qianjin Street 2699, Changchun, 130012, China

ARTICLE INFO

Keywords:
Electrochemiluminescence
MUC1
microRNA-196a
Pancreatic ductal adenocarcinoma
Biosensor
Dual targeting

ABSTRACT

Pancreatic ductal adenocarcinoma (PDAC) poses significant diagnostic challenges due to its asymptomatic nature in its early stages, low specificity of conventional *in vitro* assays, and limited efficacy of surgical interventions. However, clinical specificity of the current serum biomarkers is suboptimal, leading to diagnostic inaccuracies and oversights. Therefore, this study introduced a novel dual-target electrochemiluminescence (ECL) biosensor to address these critical issues. The ECL biosensor synergistically employs the serum biomarker MUC1 and microRNA-196a to detect early-stage PDAC precisely. While MUC1 is a differential marker between normal and cancerous pancreatic cells, its standalone diagnostic performance is limited. However, integrating miRNA-196a as a complementary marker substantially enhances the specificity of the assay. This biosensor exhibits distinct ECL signal modulation—"on-off" in the presence of MUC1 and "off-on" upon concurrent detection of MUC1 and miRNA-196a. The biosensor achieves remarkably low limits of detection (LODs) at 0.63 fg mL^{-1} and 4.57 aM for MUC1 and miRNA-196a, respectively. Thus, it facilitates the real-time differentiation between human normal pancreatic (hTERT-HPNE) and pancreatic cancer (PANC-1) cells in authentic biological matrices. This innovative approach heralds a significant advancement in the early and specific detection of PDAC, offering promising prospects for clinical translation and the broader landscape of cancer diagnostics.

1. Introduction

Pancreatic cancer (PC) is among the most lethal malignancies, and over 85% of the cases are attributed to pancreatic ductal carcinomas (PDAC) (Huang et al., 2022). Moreover, PDAC has emerged as the third leading cause of cancer-related mortality in the United States and Europe (Dalmartello et al., 2022; Guo et al., 2018; Halbrook et al., 2023). By 2040, pancreatic cancer-related deaths are predicted to exceed those from colorectal cancer, positioning it as the second leading cause of cancer-related deaths in the United States (Rahib et al., 2021). Currently, pancreatic cancer diagnosis encompasses computed tomography (CT), magnetic resonance imaging (MRI), endoscopic ultrasonography (EUS), blood analyses, and tissue biopsies (Yamada et al., 2023). Nevertheless, early-stage PDAC often manifests with non-specific symptoms and poor diagnostic specificity, leading to late-stage diagnoses and dismal prognoses (Wang et al., 2023). However, the theoretical efficacy of the aforementioned diagnostic modalities in confirming pancreatic cancer is hampered by high costs and limited specificity. Thus, the 5-year survival rate is merely 10% (Mizrahi et al., 2020).

In the pursuit of early PDAC detection, several techniques, including fluorescence imaging (Zhou et al., 2023), field-effect transistor (FET) sensing (Yu et al., 2023), and surface-enhanced Raman scattering (SERS) methodologies (Pang et al., 2019), have been explored. Electrochemiluminescence (ECL) methods stand out for their superior sensitivity and robust anti-interference capabilities (Li et al., 2023; Ye et al., 2023). The performance of ECL techniques predominantly relies on the properties of the luminescent materials employed. Thus, organic luminophores, characterized by their facile functionalization, well-defined molecular architectures, and excellent biocompatibility, have garnered significant interest in this domain (Wu et al., 2023; Zhang et al., 2021). In particular, perylene and its derivatives are preferred for their

* Corresponding author.
** Corresponding author.
E-mail addresses: mapinyi@jlu.edu.cn (P. Ma), songdq@jlu.edu.cn (D. Song).

https://doi.org/10.1016/j.bios.2024.116241
Received 12 February 2024; Received in revised form 18 March 2024; Accepted 21 March 2024
Available online 22 March 2024

exceptional stability, high quantum yields, and cost-effectiveness, making them focal points of research within the luminescent material sphere. Most perylene-based studies have been conducted in organic solvents. In contrast, perylene tetracarboxylic acid (PTCA) presents an augmented aqueous solubility with its four carboxyl groups (Zeng et al., 2018). This attribute significantly enhances the potential of PTCA as a luminescent in ECL applications, a promising avenue for developing more effective PDAC detection methodologies.

In the PDAC clinical diagnostic landscape, CA19-9, CEA, and MUC1 are commonly employed (Genco et al., 2023). Notably, CA19-9 is the sole serum biomarker for PDAC sanctioned by the U.S. Food and Drug Administration (Grunnet et al., 2015). However, its utility is compromised by the elevated expression levels in PDAC, gastric, colorectal, and cholangiocarcinoma, thereby diminishing its specificity (Luo et al. 2021, 2022). This limitation of CA19-9 underscores the need to identify biomarkers with higher specificity for the early detection of PDAC. Marker MUC1, a type I transmembrane glycoprotein, is implicated in cancer progression, particularly in pancreatic adenocarcinoma, where it is overexpressed in approximately 90% of cases (Chaika et al., 2012; Qu et al., 2004). This property makes MUC1 a potential candidate for a more specific PDAC biomarker.

Additionally, pancreatic cancer cells and tissues show aberrant microRNA (miRNA) expression profiles, with miR-196a showing significant overexpression in PDAC plasma samples (Slater et al., 2014; Tsongalis et al., 2008; Yu et al., 2017). Existing dual detection strategies mainly focus on dual-miRNA or dual-antigen detection (Jiang et al., 2023; Qi et al., 2023; Wang et al., 2021; Yu et al., 2024; Zhou et al., 2023). However, antigen detection is difficult to combine with *in vitro* amplification strategies, which greatly limits the advantages of low LOD of ECL detection. Compared with dual-miRNA detection, MUC1 has higher credibility as a serum marker already in clinical use (Yang et al., 2020). Therefore, integrating MUC1 with miR-196a could potentially refine the specificity of PDAC detection assays, enhancing early diagnosis capabilities.

This study involved an enzyme-mediated "on-off-on" ECL biosensor tailored for the precise detection of PDAC, employing silver-decorated perylene tetracarboxylic acid (Ag@PTCA) as the luminophore. The PTCA was self-assembled and subsequently adorned with silver nanoparticles (Ag NPs) to yield the Ag@PTCA composite (refer to Scheme 1A). Herein, PTCA serves as the luminophore, $S_2O_8^{2-}$ acts as a co-reactant enhancer, while the incorporated Ag, a noble metal, fulfils the dual roles of catalyzing reactions and augmenting the conductivity of the material. Incorporating Ag into PTCA facilitates expedited electron transfer, thereby amplifying the sensitivity of the biosensor (Scheme 1B). As depicted in Scheme 1C, the biosensor employs a strand displacement reaction (SDR) mechanism, enabling the generation of multiple MT oligonucleotide chains upon interaction with the target MUC1 biomarker. The thiol groups (-SH) on the MT chains facilitate binding to Ag NPs via Ag–S bonds. Concurrently, the ferrocene (Fc) moieties tagged at the opposite ends of MT chains impede electron transfer, diminishing ECL intensity (Scheme 1E). A reduction in the ECL intensity signifies the detection of the target PDAC biomarker, MUC1. The introduction of miRNA-196a further refines the assay, triggering a secondary reaction cycle (Scheme 1D). In the secondary reaction cycle, miRNA-196a associates with the HP oligonucleotide strand, enabling T7 exonuclease (T7 EXO) to excise the double-stranded segment of the HP strand, releasing the ST strand. The liberated ST strand subsequently attaches to the electrode-bound MT chain, forming a duplex. Next, T7 EXO cleaves at the 5′ end of the MT chain, dislodging the Fc moiety and reinstating the ECL intensity (Scheme 1E). This dual-recognition strategy, coupling MUC1 with miRNA-196a, ensures PDAC-specific detection. Furthermore, leveraging the enzymatic processes enhances the simplicity and sensitivity of the biosensor compared to non-enzymatic approaches, achieving impressive detection thresholds of 0.63 fg mL^{-1} for MUC1 and 4.57 aM for miRNA-196a. This strategy provides a new ultrasensitive and deliberate method for early detection of PDAC, with a broad application prospect in early cancer screening.

2. Experimental section

2.1. Synthesis of Ag@PTCA

Perylene tetracarboxylic acid was synthesized with reference to published literature (Zeng et al., 2018) (see supporting information for

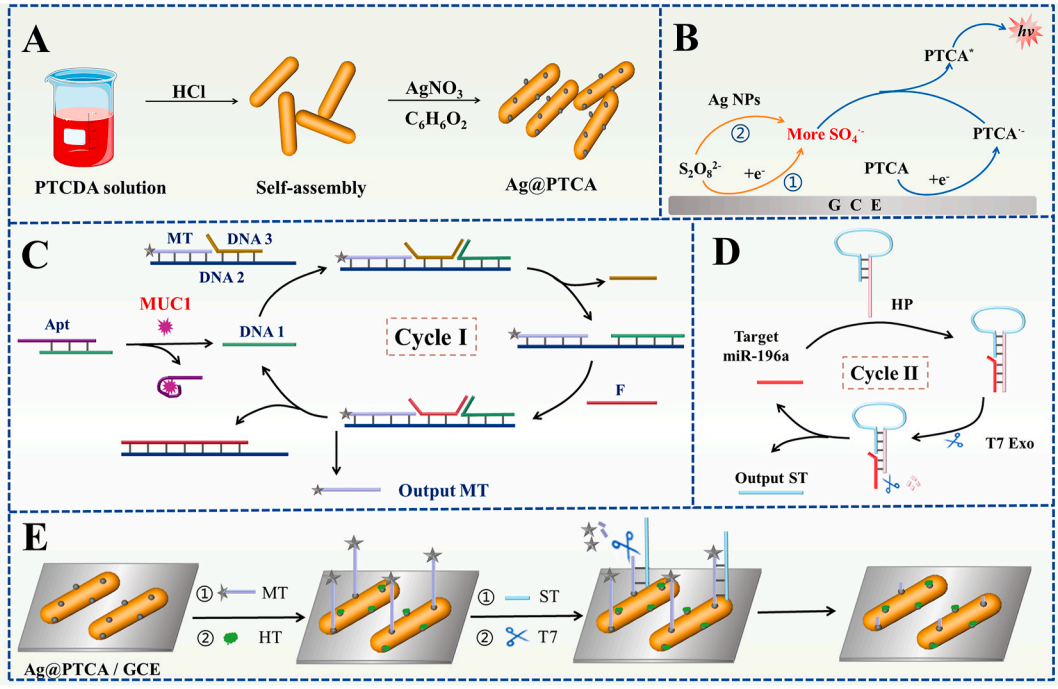

Scheme 1. (A) Illustration of Ag@PTCA; (B) Luminescence mechanism of the ECL biosensor; (C) SDR signal amplification process; (D) T7 EXO-driven signal amplification process; (E) The construction of the signal "on-off-on" mode biosensor for detecting MUC1 and miRNA-196a.

specific synthesis steps). The obtained solid PTCA was dispersed into deionized water to obtain a 100 μg/mL solution. Then, 5 mL of the solution was mixed with 50 μg of $Ag(NO)_3$ with rapid stirring for 2 h. Subsequently, hydroquinone was added dropwise under ultrasonic conditions until the solution became discolored. Next, centrifugation was performed to remove surplus reagent, and the resulting sample was dispersed into water and set aside.

2.2. Preparation of the reaction solution

All the oligonucleotides (Apt, DNA 1, DNA 2, DNA 3, F, and MT) in the SDR section were dissolved separately in Tris-HCl buffer to obtain the stock solution. Equal volumes of equal concentrations of DNA 1 and Apt strands were annealed at 95 °C and then slowly cooled to room temperature to obtain DNA 1/Apt double-stranded complexes. Then, different concentrations of MUC1 protein and double-stranded complexes were mixed and incubated at 37 °C for 2 h to obtain the product solution. Next, equal volumes and concentrations of DNA 2, DNA 3, and MT strands were mixed, and the resulting mixture was annealed at 95 °C for 5 min before being slowly cooled to room temperature to form a three-stranded DNA complex. Finally, the product solution (2 μM) was mixed with the F strand (0.5 μM) and the three-stranded DNA complex (2 μM) and incubated at 37 °C for 85 min to obtain the SDR reaction solution.

The T7 EXO reaction solution was prepared by mixing different concentrations of the miRNA-196a strand, incubated with HP strand (2.5 μM) for 2 h at 37 °C, and topped with T7 EXO (100 U mL^{-1}).

2.3. Construction of the ECL biosensor

The GCE was polished with 0.3 μM and 0.5 μM alumina powder and then sonicated with ethanol and ultrapure water to remove the residual alumina powder, obtaining a clean electrode interface. The treated GCE was air-dried, and 10 μL Ag@PTCA (0.012 mg mL^{-1}) was added dropwise to the electrode surface and dried at 37 °C for 2 h. Next, 10 μL of the SDR reaction solution was added dropwise to the surface of the modified electrode and incubated at 37 °C for 2 h. The electrode was washed using a trickle of deionized water to remove the incompletely bound DNA. Then, the nonspecific binding site was closed with HT (1 μM) and incubated at 37 °C for 40 min. The sensor detected the miRNA-196a part, and the electrode was washed with a trickle of deionized water after sealing the non-specific binding site with HT. Then, 10 μL of the T7 EXO reaction solution was added dropwise to the electrode and incubated for 4 h at 25 °C. At the end of the reaction, the electrode was placed in an oven at 80 °C for 30 min to inactivate the T7 EXO.

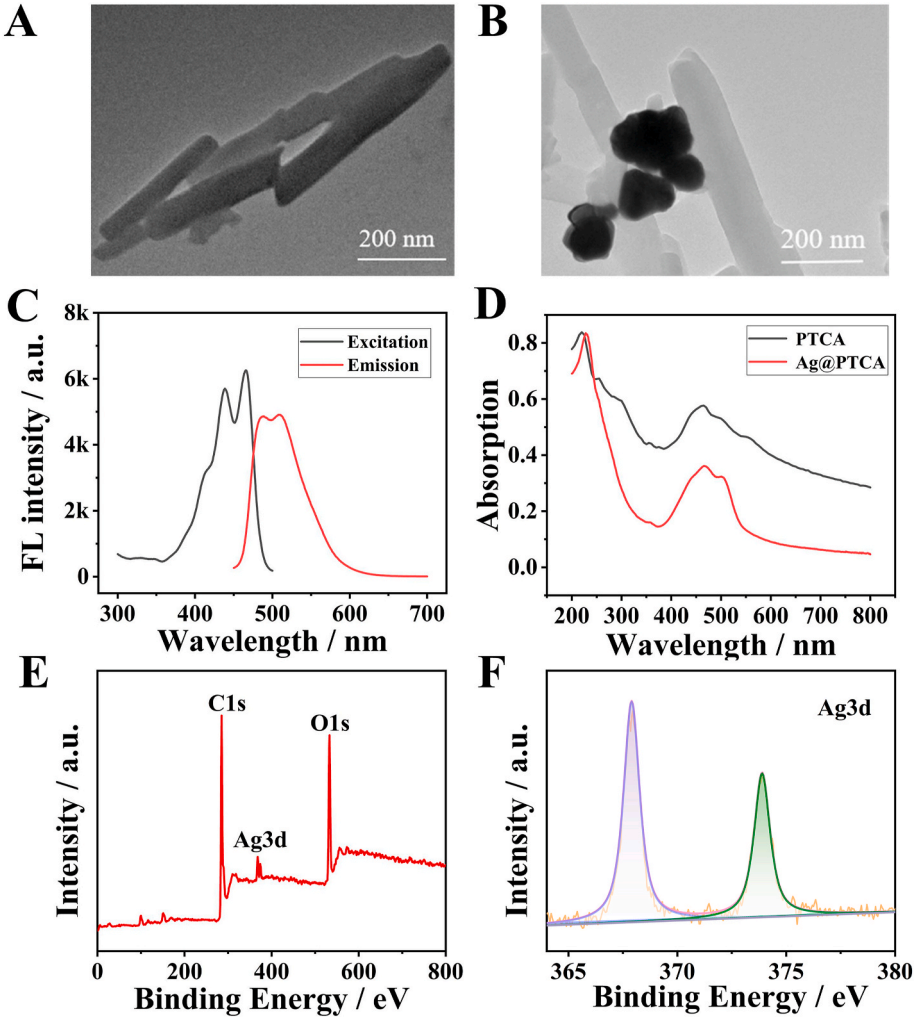

Fig. 1. (A) TEM morphology of PTCA. (B) TEM morphology of Ag@PTCA. (C) Fluorescence spectra of PTCA. (D) UV absorption spectra of PTCA (black line) and Ag@PTCA (red line). (E) XPS scans for the full region of Ag@PTCA. (F) XPS scans for Ag3d regions.

3. Results and discussion

3.1. Characterization of PTCA and Ag@PTCA

First, the morphologies of the prepared PTCA and Ag@PTCA were characterized using transmission electron microscopy (TEM). The PTCA nanomaterials showed a short rod shape (Fig. 1A), consistent with previous literature reports (Li et al., 2019; Zhang et al., 2018). The morphology of PTCA after surface loading of Ag NPs shows that the Ag NPs are distributed around the PTCA (Fig. 1B).

Furthermore, the fluorescence excitation and emission spectra of PTCA (Fig. 1C) are consistent with previous literature, proving that PTCA was successfully synthesized (Goswami et al., 2021). The UV absorption spectra (Fig. 1D) of PTCA and Ag@PTCA show that the PTCA absorption peak at 220 nm is caused by the π-π* jump of the perylene-conjugated system (Chen et al., 2021). Due to the extension of the conjugated system, the absorption band shifts to the visible region, forming two visible absorption peaks, 465 nm and 500 nm.

Further, loading Ag NPs caused a slight red-shifting of the overall UV spectral peaks, but the peak shapes did not change significantly, proving that the particle size of the material had changed. The Ag 3 d, O 1s, and C 1s peaks (Fig. 1E and F) in the X-ray photoelectron spectroscopy (XPS) confirmed the chemical content of Ag@PTCA, further confirming that Ag NPs were successfully loaded onto PTCA. The binding energies corresponding to the C–C, C–O, C═O, and O–C═O groups (Fig. S6A) and O–H, O–C═O, and C–O groups (Fig. S6B) are consistent with the reported literature (Chai et al., 2022; Song et al., 2019). Therefore, the above peaks can be attributed to the hydroxyl groups in PTCA. This study successfully synthesized PTCA nanorods and loaded Ag NPs on top of the nanorods to form the Ag@PTCA structure.

3.2. The mechanism of the Ag@PTCA + $S_2O_8^{2-}$ ECL reaction system

The ECL responses of the PTCA (curve a), PTCA + $S_2O_8^{2-}$ (curve b), Ag NPs + PTCA + $S_2O_8^{2-}$ (curve c), and Ag@PTCA + $S_2O_8^{2-}$ (curve d) solutions were examined to investigate the mechanism of Ag@PTCA + $S_2O_8^{2-}$ system (Fig. 2A). There was no observable ECL intensity response after incubating PTCA on the GCE surface in deionized water (curve a). When GCE was detected in the $K_2S_2O_8$ solution, the ECL intensity was significantly enhanced, mainly because $K_2S_2O_8$, a PTCA co-reactant, reacted with $PTCA^-$ to produce PTCA*, thus enhancing the ECL intensity. Moreover, Ag NPs, a noble metal, have good electrical conductivity and can react with $S_2O_8^{2-}$ to produce more $SO_4^{\cdot-}$. Thus, curve c has a significantly stronger ECL intensity than curve b. Therefore, curve d showed a stronger ECL intensity than curve c because Ag NPs are loaded on the surface of PTCA, shortening the electron transport distance and enhancing the ECL intensity.

The following equations show the ECL enhancement mechanism of this ECL system (Lei et al., 2018):

$$PTCA + e^- \rightarrow PTCA^{\cdot-} \quad (1)$$

$$S_2O_8^{2-} + e^- \rightarrow SO_4^{\cdot-} \quad (2)$$

$$PTCA^{\cdot-} + SO_4^{\cdot-} \rightarrow PTCA^* + SO_4^{2-} \quad (3)$$

$$PTCA^* \rightarrow PTCA + h\nu \quad (4)$$

Fig. 2B shows that loading Ag NPs enhances and stabilizes the ECL intensity. Equations (5)–(12) (below) further explored the principle of Ag NPs as efficient co-reactants for this system, hypothesizing the efficiency may be due to the large amount of $SO_4^{\cdot-}$ produced in the two lines. In turn, the generated $SO_4^{\cdot-}$ can react with the luminophore PTCA to produce more excited-state PTCA*, producing a powerful ECL intensity. This work also compared the loading of different noble metals on the luminophore PTCA (Fig. 2C) to verify further the enhancement mechanism of Ag NPs on PTCA/$S_2O_8^{2-}$. The enhancement effect of Ag NPs on the PTCA/$S_2O_8^{2-}$ system is significantly stronger than that of Au NPs, Pt NPs, and Pd NPs.

The following equations show the catalytic mechanism of Ag NPs for this ECL system (Al-Shehri et al., 2021):

$$Ag^0 + Ag^+ \rightarrow Ag^0\text{-}\,Ag^+ \quad (5)$$

$$2\,Ag^0 - Ag^+ \rightarrow Ag_2^+ - Ag_2^+ \quad (6)$$

$$S_2O_8^{2-} + (Ag_2^+ - Ag_2^+) \rightarrow Ag^{2+} + SO_4^{2-} + Ag_2^+ + Ag^0 + SO_4^{\cdot-} \quad (7)$$

$$2\,Ag^{2+} + H_2O \rightarrow Ag^+ + AgO^+ + 2H^+ \quad (8)$$

$$AgO^+ + H_2O \rightarrow Ag^+ + H_2O_2 \quad (9)$$

$$H_2O_2 + e^- \rightarrow OH^- + OH^{\cdot} \quad (10)$$

$$OH^{\cdot} + S_2O_8^{2-} \rightarrow SO_4^{\cdot-} + HSO_4^- + O_2 \quad (11)$$

$$O_2 + H_2O + e^- \rightarrow OH^- + H_2O_2 \quad (12)$$

3.3. The feasibility of target cycling

Gel electrophoresis was used to characterize the cyclic amplification process of the target. The bands in lanes 1 and 2 represent the Apt and DNA 1 strands, respectively (Fig. S5A). When the Apt and DNA 1 strands were mixed and annealed, a bright band appeared in lane 3, representing the double-stranded Apt/DNA 1 formed by the hybridization of the Apt and DNA 1 strands. After adding the target MUC1 into the double-stranded solution, MUC1 bound with the Apt strand to form the MUC1-Apt complex, and more DNA 1 strands were produced, which matched with the bands in lane 4.

Lanes 1, 2, 3, and 4 represent DNA 1, DNA 3, MT, and F strands, respectively (Fig. S5B). When the DNA 2, DNA 3, and MT strands were mixed and annealed, a bright band appeared in lane 5, representing a three-strand complex formed by the hybridization of the DNA 2, DNA 3, and MT strands. Further, adding the DNA 1 strand causes it to bind to the

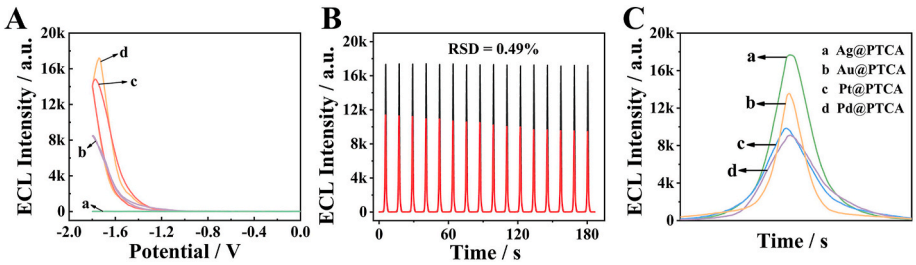

Fig. 2. (A) ECL intensity of (a) PTCA in H_2O, (b) PTCA, (c) PTCA + Ag NPs, and (d) Ag@PTCA in 10 mM $S_2O_8^{2-}$ during potential scanning between −1.8 and 0 V (scan rate: 0.3 V/s). (B) ECL intensity of PTCA (red line) and Ag@PTCA (blank line). (C) ECL intensity of (a) Ag@PTCA, (b) Au@PTCA, (c) Pt@PTCA, and (d) Pd@PTCA.

three-stranded complex, crowding out the DNA 3 strand and creating a bright band in lane 6 and the corresponding band for the DNA 3 strand. Next, adding the F strand caused it to bind to the DNA 2 strand to form a double-stranded complex, corresponding to the bright band in lane 8. Therefore, adding the DNA 1 and F strands to the three-stranded complex produced a hybridized strand of the DNA 2 and the F strands, which crowded out the other strands. The bands in lane 7 are consistent with the expected results.

Lanes 1, 2, and 3 represent the HP, MT, and target miRNA-196a strands, respectively (Fig. S5C). After adding the target miRNA-196a strand to the HP strand, a bright band appeared in lane 4, representing the double-stranded HP/miRNA-196a formed by the HP-miRNA-196a hybridization. T7 EXO can be specifically digest the DNA strand in DNA/RNA hybrid into a single base in the 5′→3′ direction, and then releasing RNA for additional cycling amplification (Shen et al., 2022). There, Lane 5 represents the double-stranded portion of the HP strand bound to the target miRNA-196a strand was sheared off by T7 EXO, dropping out the ST and miRNA-196a strands and making the dropped miRNA-196a strand available for the next cycle. Lane 6 is the ST strand alone. Lane 7 represents the double strand formed by the ST and MT strand hybridization after annealing. Finally, lane 8 shows that the MT and ST strands hybridized with the part of the double strand that was sheared off after the T7 Exo addition. From the gel electrophoresis results, the hypothesis is that the cyclic amplification of the target proceeded as expected.

3.4. Characterization of ECL biosensors

The preparation of the ECL biosensor was characterized by CV and EIS, respectively. Fig. 3A demonstrates the current-effect values of the electrode in $[Fe(CN)_6]^{3-/4-}$(5 mM) solution containing 0.1 M KCl during biosensor assembly. The bare electrode (curve a) shows a pair of clear and reversible redox peaks. The peak currents changed when the electrode was modified with PTCA (curve b). However, when the electrode was modified with Ag@PTCA (curve c), the peak current was enhanced due to the strong conductivity of Ag. The redox peak currents decreased sequentially after hybridization with SDR (curve d) and HT (curve e). Furthermore, the redox peak current increases after the T7 EXO reaction (curve f), possibly because T7 EXO shears off the ferrocene on the MT chain, increasing the current response.

Besides, EIS can also be used to characterize the ECL biosensor assembly. As shown in Fig. 3B, the EIS curve of the bare electrode (curve a) is a smaller semicircle, indicating a smaller impedance. When the electrode was modified by the PTCA (curve b), the impedance of this electrode increased slightly. Nonetheless, when Ag@PTCA modifies the (curve c) electrode, Ag increases the conductivity of the electrode and facilitates electron transfer, resulting in a smaller semicircle diameter for this curve. The ferrocene on the MT chain solid-loaded SDR product (curve d) hinders the electron transfer at the electrode surface, increasing the electrode impedance. Closing the nonspecific binding site on the modified electrode with HT (curve e) further increased the semicircle diameter in the resulting EIS curve, indicating a continuous increase in impedance. However, the semicircle diameter in the EIS curves decreased when the T7 EXO shearing reaction (curve f) occurred on the electrode surface, indicating a decrease in its impedance. The decrease is mainly because T7 EXO sheared off the ferrocene on the MT chain on the electrode surface. Thus, the CV and EIS results demonstrate that the ECL biosensor assembly is as expected.

3.5. Optimization of experimental conditions

The reaction time and concentration of T7 EXO were optimized in this experiment to achieve the best test performance. The ECL intensity gradually enhanced and leveled off at around 4 h with increasing T7 EXO incubation time at the electrode (Fig. S4A). Furthermore, the ECL intensity gradually enhanced with the increase of T7 EXO concentration until around 100 U mL^{-1}, when the enhancement ceased (Fig. S4B). Therefore, 4 h and 100 U mL^{-1} were selected as the optimal reaction time and concentration, respectively.

3.6. Detection of the designed biosensor

The sensor was quantitatively tested under optimal conditions. Fig. 4A and B shows that the ECL intensity of the sensor gradually weakened as the concentration of the target MUC1 increased from 1 fg mL^{-1} to 100 ng mL^{-1}. The standard curve showed a good linear relationship between the ECL response and the logarithmic value of the target concentration. Thus, the linear regression equation was $I_1 = -1813.97\ lgc_1 + 5513.94$ (I_1 represents the ECL intensity and c_1 represents the MUC1 concentration), with a correlation coefficient of $R_1^2 = 0.9993$, and a detection limit of 0.63 fg mL^{-1} (S/N = 3).

For further quantitative analysis of the target miRNA-196a, the concentration of MUC1 was first controlled at 100 ng mL^{-1}. Then, different concentrations of miRNA-196a, T7 EXO (100 U mL^{-1}), and HP (2.5 μM) were added dropwise to the electrodes and incubated at 25 °C for 4 h. The results showed that increasing the concentration of the target miRNA-196a from 100 aM to 1 nM gradually enhanced the ECL intensity of the sensor (Fig. 4C and D). The standard curve showed a good linear relationship between the ECL response and the logarithmic value of the target concentration.

The linear regression equation was $I_2 = 1166.30\ lgc_2 + 15135.24$ (I_2 represents the ECL intensity and c_2 represents the miRNA-196a concentration), with a correlation coefficient of $R_2^2 = 0.9989$, and a detection limit of 4.57 aM (S/N = 3). A comparison of the biosensor prepared in this experiment with other published literature (Supporting Information, Table S2) showed that the biosensor had a lower detection limit and better sensitivity.

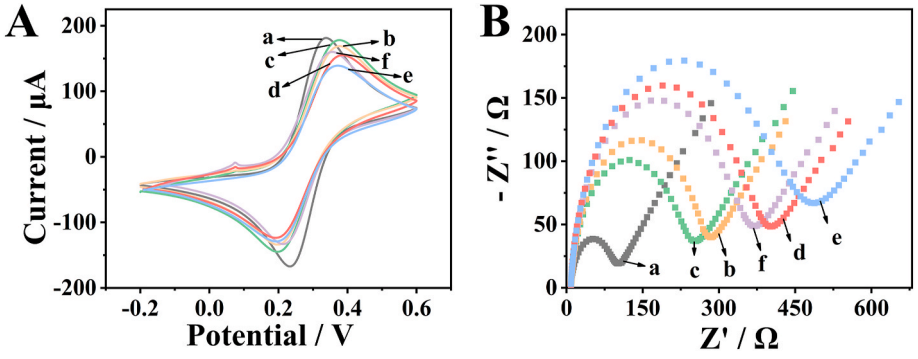

Fig. 3. (A) Typical cyclic voltammetry (CV) and (B) electrochemical impedance spectroscopy (EIS) responses of: (a) bare GCE, (b) PTCA/GCE, (c) Ag@PTCA/GCE, (d) SDR/Ag@PTCA/GCE, (e) HT/SDR/Ag@PTCA/GCE, and (f) T7/HT/SDR/Ag@PTCA/GCE.

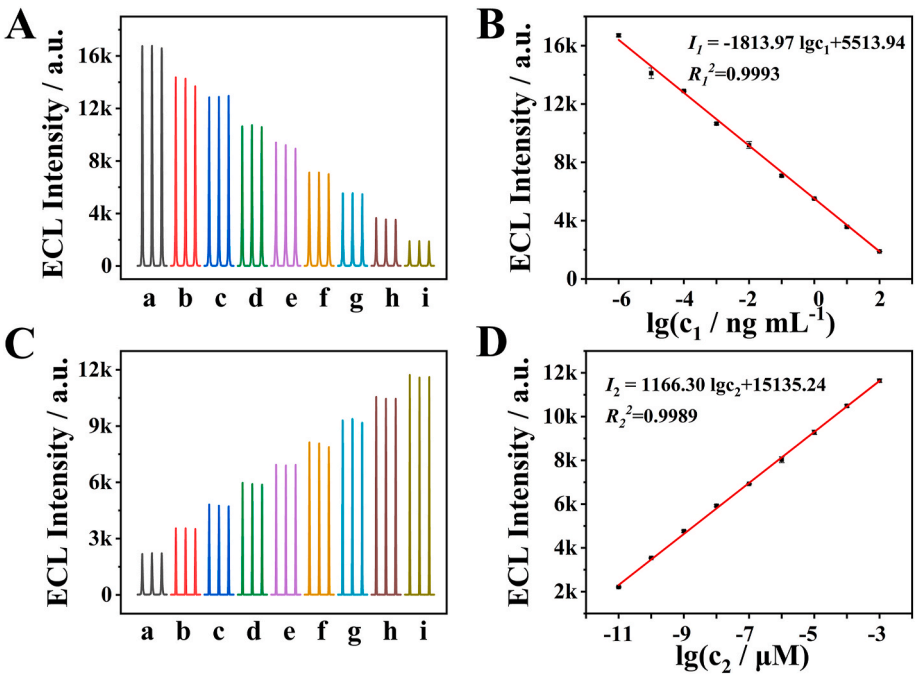

Fig. 4. (A) ECL response of different MUC1 concentrations based on the developed biosensor. (B) Liner calibration plots for the I_1 intensity and lgc$_1$ (c$_1$: the concentration of target MUC1). (C) ECL response of different miRNA-196a concentrations based on the developed biosensor. (D) Liner calibration plot for the I_2 intensity and lgc$_2$ (c$_2$: the concentration of target miRNA-196a).

3.7. Specificity and stability of the biosensor

The selectivity and stability of the ECL biosensor are important feasibility indicators. First, the study evaluates the selectivity of the constructed sensor for the MUC1 protein. Therefore, CEA, lgG, BSA, and hGH were used as interfering substances to replace MUC1 for comparison experiments (Fig. 5A). The ECL intensity obtained from electrodes incubated with blank solution were similar to those obtained from electrodes incubated with CEA (100 ng mL^{-1}), lgG (100 ng mL^{-1}), BSA (100 ng mL $^{-1}$), and hGH (100 ng mL^{-1}). Moreover, the ECL intensity obtained by incubating the electrodes with the reaction solution prepared by mixing the above-interfering substances with MUC1 (1 ng mL^{-1}) did not differ significantly from that obtained by incubating MUC1 (1 ng mL^{-1}) alone. These results indicated that CEA, lgG, BSA, and hGH did not significantly affect MUC1 detection.

Next, miRNA-105, miRNA-141, miRNA-155, and miRNA-210 were selected as interfering substances to replace miRNA-196a for the comparison experiments. The electrodes incubated with a blank solution produced similar ECL intensity as those incubated with miRNA-105 (100 nM), miRNA-141 (100 nM), miRNA-155 (100 nM), and miRNA-210 (100 nM) (Fig. 5B). Incubating the above-interfering substances mixed with miRNA-196a (1 nM) to form a reaction solution on the surface of the electrodes resulted in a stronger ECL intensity, similar to the ECL intensity obtained by incubating miRNA-196a (1 nM) alone. These results showed that miRNA-105, miRNA-141, miRNA-155, and miRNA-210 had no significant effect on the miRNA-196a detection. In summary, the sensor prepared in this experiment has good selectivity for detecting MUC1 and miRNA-196a.

When the concentration of the target MUC1 was 100 ng mL^{-1}, the ECL intensity of this sensor did not change significantly (RSD = 1.55%), even with 16 consecutive scans (Fig. 5C). Additionally, 1 nM of the target miRNA-196a (Fig. 5D) did not significantly change the ECL intensity of this sensor, even with 16 consecutive scans (RSD = 0.83%). These results indicate that the sensor prepared in this experiment has good stability.

3.8. Application of biosensor in real samples

The lysates of human normal pancreatic cells (hTERT-HPNE), human pancreatic adenocarcinoma cells (PANC-1), and human hepatocellular carcinoma cells (HepG-2) were used as the reaction solution to investigate the expression of MUC1 and miRNA-196a. Because of the proximity of the liver to the pancreas and the potential for confusion during early presentation and detection, HepG-2 cells were chosen as a control group. The ECL intensity gradually decreased with the increase of the PANC-1 cells, whereas the ECL intensity of HepG-2 and HPNE cells did not change significantly (Fig. 5E) (Dong et al., 2022). Therefore, this part of the test can rule out the possibility of hepatocellular carcinoma in the samples. As shown in the second cycle (Fig. 5F), the ECL intensity gradually increased with the number of PANC-1 cells. This trend indicates that the MUC1 protein and miRNA-196a were highly expressed in PANC-1 cells, matching with previous related literature (Cheng et al., 2014). The above results demonstrated that the biosensor constructed in this experiment has excellent selectivity.

Next, standard samples with different MUC1 protein and miRNA-196a concentrations were prepared using the standard addition method with a 100-fold diluted healthy human serum solution. The purpose was to further validate the feasibility of the biosensor for detecting MUC1 protein and miRNA-196a in human serum samples. The ECL intensity was used to calculate the corresponding concentrations according to the standard curve, and the ratio between this calculated and the standard concentration was the recovery (Supporting Information Table S4). The obtained recoveries ranged from 99.64 to 102.52%.

4. Conclusion

In summary, this study synthesized the ECL luminophore PTCA using the self-assembly method simply and efficiently, the basis of which the study optimized the luminophores to enhance their luminous efficiency and stability. Furthermore, this study developed an enzyme-driven ECL biosensor that utilizes Ag@PTCA as an electrochemical luminescent material for the specific detection of the PDAC biomarkers MUC1 and miRNA-196a. These markers trigger the SDR and output MT chain to

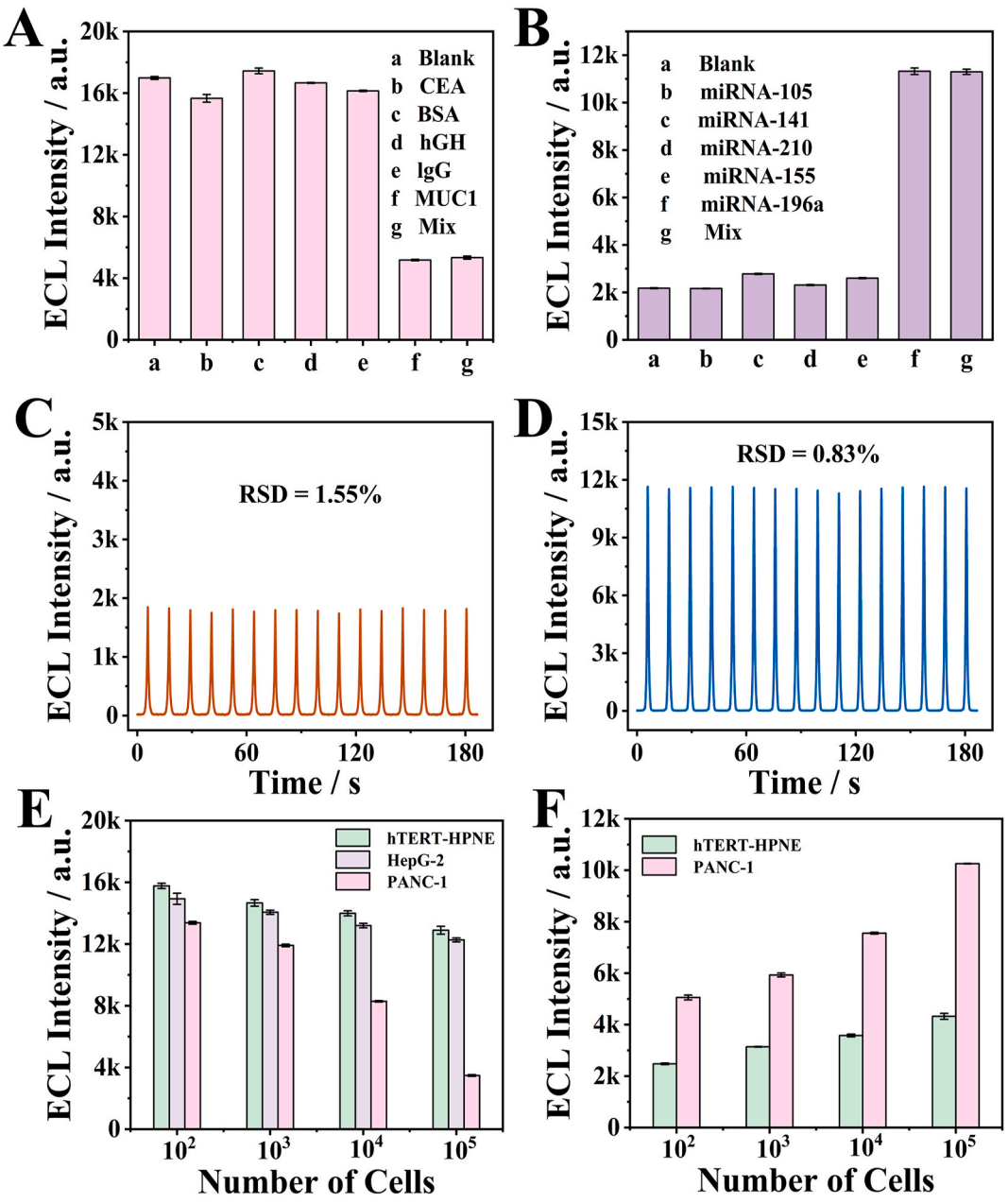

Fig. 5. Stability (A, B) and selectivity (C, D) of the designed ECL biosensor. (E) ECL biosensor detects MUC1 in different cells (hTERT-HPNE, HepG-2, and PANC-1). (F) ECL biosensor detects miR-196a in different cells (hTERT-HPNE and PANC-1).

generate the ECL response in the presence of MUC1 but cannot trigger SDR in the absence of MUC1. When both MUC1 and miRNA-196a are present, the ECL response can be generated in a "turn off-on" mode, explicitly identifying the human normal (hTERT-HPNE) and pancreatic cancer (PANC-1) cells. This strategy provides a new pathway for the ultrasensitive detection of biomolecules in PDAC and facilitates the early diagnosis and treatment of PDAC.

CRediT authorship contribution statement

Yuxuan Chen: Writing – original draft, Investigation, Formal analysis, Data curation, Conceptualization. **Zhuoxin Ye:** Investigation, Data curation. **Mo Ma:** Investigation, Formal analysis. **Jukun Yang:** Investigation, Data curation. **Ruiyan Liu:** Methodology, Investigation. **Yan Zhang:** Methodology, Investigation. **Pinyi Ma:** Writing – review & editing, Project administration, Data curation, Conceptualization. **Daqian Song:** Supervision, Resources, Funding acquisition, Conceptualization.

Declaration of competing interest

The authors declare that they have no known competing financial interests or personal relationships that could have appeared to influence the work reported in this paper.

Data availability

Data will be made available on request.

Acknowledgments

This work was supported by the National Natural Science Foundation

of China (22074052 and 22004046) the Science and Technology Developing Foundation of Jilin Province of China (Nos. 20240404044 ZP,20230101033JC, and 20230204116YY).

Appendix A. Supplementary data

Supplementary data to this article can be found online at https://doi.org/10.1016/j.bios.2024.116241.

References

Al-Shehri, A.S., Zaheer, Z., Alsudairi, A.M., Kosa, S.A., 2021. ACS Omega 6 (41), 27510–27526.

Chai, D.-D., Zhuo, Y., Tu, T.-T., Li, H.-L., Yuan, R., Wei, S.-P., 2022. Anal. Chem. 94 (27), 9934–9939.

Chaika, N.V., Gebregiworgis, T., Lewallen, M.E., Purohit, V., Radhakrishnan, P., Liu, X., Zhang, B., Mehla, K., Brown, R.B., Caffrey, T., Yu, F., Johnson, K.R., Powers, R., Hollingsworth, M.A., Singh, P.K., 2012. Proc. Natl. Acad. Sci. 109 (34), 13787–13792.

Chen, X., Zhang, D., Lin, H., Wei, W., Hao, T., Hu, Y., Wang, S., Guo, Z., 2021. Sens. Actuators B Chem. 346, 130549.

Cheng, J.Q., Huang, F., Tang, J., Zhuang, X., Zhuang, Y., Cheng, W., Chen, W., Yao, H., Zhang, S., 2014. PLoS One 9 (2), e87897.

Dalmartello, M., La Vecchia, C., Bertuccio, P., Boffetta, P., Levi, F., Negri, E., Malvezzi, M., 2022. Ann. Oncol. 33 (3), 330–339.

Dong, Q., Jia, X., Wang, Y., Wang, H., Liu, Q., Li, D., Wang, J., Wang, E., 2022. J. Nanobiotechnol. 20 (94), 1–12.

Genco, E., Modena, F., Sarcina, L., Björkström, K., Brunetti, C., Caironi, M., Caputo, M., Demartis, V.M., Di Franco, C., Frusconi, G., Haeberle, L., Larizza, P., Mancini, M.T., Österbacka, R., Reeves, W., Scamarcio, G., Scandurra, C., Wheeler, M., Cantatore, E., Esposito, I., Macchia, E., Torricelli, F., Viola, F.A., Torsi, L., 2023. Adv. Mater. 35 (42), 2304102.

Goswami, T., Bheemaraju, A., Kataria, A., Nag, A., Sravani, K., Mishra, S., Mishra, A.K., 2021. Mater. Chem. Phys. 259, 124086.

Grunnet, M., Christensen, I.J., Lassen, U., Jensen, L.H., Lydolph, M., Knox, J.J., McNamara, M.G., Jitlal, M., Wasan, H., Bridgewater, J., Valle, J.W., Mau-Sorensen, M., 2015. Eur. J. Cancer 51 (11), 1381–1388.

Guo, S., Fesler, A., Wang, H., Ju, J., 2018. Biomark. Res. 6 (18), 1–5.

Halbrook, C.J., Lyssiotis, C.A., Pasca di Magliano, M., Maitra, A., 2023. Cell 186 (8), 1729–1754.

Huang, X., Zhang, G., Liang, T., 2022. Trends pharmacol. Sci 43 (6), 482–494.

Jiang, P., Bai, Y., Yan, L., Feng, P., Huang, K., Chen, J., Chen, P., 2023. Anal. Chem. 95 (19), 7676–7684.

Lei, Y.-M., Wen, R.-X., Zhou, J., Chai, Y.-Q., Yuan, R., Zhuo, Y., 2018. Anal. Chem. 90 (11), 6851–6858.

Li, H., Yang, Q., Wang, Z., Li, F., 2023. ACS Sens. 8 (4), 1529–1535.

Li, P., Wang, J., Chen, H., Sun, X., You, J., Liu, S., Zhang, Y., Liu, M., Niu, X., Luo, Y., 2019. J. Mater. Chem. A 7 (20), 12446–12450.

Luo, G., Jin, K., Deng, S., Cheng, H., Fan, Z., Gong, Y., Qian, Y., Huang, Q., Ni, Q., Liu, C., Yu, X., 2021. Biochim. Biophys. Acta, Rev. Cancer 1875 (2), 188409.

Luo, K., Zhao, C., Luo, Y., Pan, C., Li, J., 2022. Biosens. Bioelectron. 216, 114672.

Mizrahi, J.D., Surana, R., Valle, J.W., Shroff, R.T., 2020. Lancet. 395 (10242), 2008–2020.

Pang, Y., Wang, C., Lu, L., Wang, C., Sun, Z., Xiao, R., 2019. Biosens. Bioelectron. 130, 204–213.

Qi, L., Zhang, X., Wu, R., Fang, Q., Yu, J., Hu, X., Chen, L., Shang, X., Sun, X., Zhou, P., Si, J., Wang, Z., Jiang, Y., Du, Y., 2023. Anal. Chem. 95 (15), 6433–6440.

Qu, C.F., Li, Y., Song, Y.J., Rizvi, S.M.A., Raja, C., Zhang, D., Samra, J., Smith, R., Perkins, A.C., Apostolidis, C., Allen, B.J., 2004. Brit. J. Cancer 91 (12), 2086–2093.

Rahib, L., Wehner, M.R., Matrisian, L.M., Nead, K.T., 2021. JAMA Netw. Open 4 (4), e214708.

Shen, B., Wu, Q., Fan, Y., Wu, H., Li, X., Zhao, X., Wang, Y., Ding, S., Zhang, J., 2022. Chem. Eng. J. 445.

Slater, E.P., Strauch, K., Rospleszcz, S., Ramaswamy, A., Esposito, I., Klöppel, G., Matthäi, E., Heeger, K., Fendrich, V., Langer, P., Bartsch, D.K., 2014. Transl Oncol 7 (4), 464–471.

Song, X., Li, X., Wei, D., Feng, R., Yan, T., Wang, Y., Ren, X., Du, B., Ma, H., Wei, Q., 2019. Biosens. Bioelectron. 126, 222–229.

Tsongalis, G.J., Labourier, E., Hahn, S.A., Korc, M., Tannapfel, A., Marc Pipas, J., Suriawinata, A.A., Gutmann, E.J., Barth, R.J., Munding, J.B., Luttges, J., Gordon, S., Edmunds, H.S., Doleshal, M., Szafranska, A.E., 2008. Clin. Chem. 54 (10), 1716–1724.

Wang, N., Chen, L., Chen, W., Ju, H., 2021. Anal. Chem. 93 (12), 5327–5333.

Wang, Q., Šabanović, B., Awada, A., Reina, C., Aicher, A., Tang, J., Heeschen, C., 2023. Eur. J. Cancer 190, 112940.

Wu, K., Zheng, Y., Chen, R., Zhou, Z., Liu, S., Shen, Y., Zhang, Y., 2023. Biosens. Bioelectron. 223, 115031.

Yamada, R., Tsuboi, J., Murashima, Y., Tanaka, T., Nose, K., Nakagawa, H., 2023. Biomedicines 11 (6), 1687.

Yang, L., Yin, X., An, B., Li, F., 2020. Anal. Chem. 93 (3), 1709–1716.

Ye, Z., Liu, Y., Pan, M., Tao, X., Chen, Y., Ma, P., Zhuo, Y., Song, D., 2023. Biosens. Bioelectron. 228, 115219.

Yu, J., Liu, Q., Qi, L., Fang, Q., Shang, X., Zhang, X., Du, Y., 2024. Biosens. Bioelectron. 252, 116137.

Yu, Q., Xu, C., Yuan, W., Wang, C., Zhao, P., Chen, L., Ma, J., 2017. BioMed Res. Int. 2017, 1–10.

Yu, Y., Liang, C., Wan, Q.-Q., Jin, D., Liu, X., Zhang, Z., Sun, Z.-Y., Zhang, G.-J., 2023. Anal. Chim. Acta 1284, 341995.

Zeng, W.-J., Liao, N., Lei, Y.-M., Zhao, J., Chai, Y.-Q., Yuan, R., Zhuo, Y., 2018. Biosens. Bioelectron. 100, 490–496.

Zhang, H., Zuo, F., Tan, X., Xu, S., Yuan, R., Chen, S., 2018. Biosens. Bioelectron. 104, 65–71.

Zhang, X., Wang, P., Nie, Y., Ma, Q., 2021. TrAC-Trend. Anal. Chem 143, 116410.

Zhou, J., Liu, F., Han, Y., Li, H., Wei, S., Ouyang, Y., Chai, Y., Yuan, R., 2023. Anal. Chem. 95 (39), 14558–14565.